JOURNAL OF COMPUTATIONAL PHYSICS **128,** 489–497 (1996)
ARTICLE NO. 0226

The ARCTIC Charged Particle Beam Propagation Code

MICHAEL A. MOSTROM, DUSHAN MITROVICH, AND DALE R. WELCH

Mission Research Corporation, 1720 Randolph Road SE, Albuquerque, New Mexico 87106-4245

Received January 27, 1995; revised May 1, 1996

The ARCTIC code has been developed to calculate the inductive erosion of, and plasma wakefield generation by, an ultrarelativistic electron beam propagating in a straight ionized channel through a background plasma. The implicit algorithm used is described in detail, and the code is verified by comparing results with a more complete full particle-in-cell plasma simulation code.

I. INTRODUCTION

As a highly relativistic (effectively rigid) electron beam moves through a neutral plasma, the excess negative charge introduced by the beam produces a radial electric field that expels the plasma electrons from the vicinity of the beam. This outward plasma electron flow near the front of the beam gives rise to a longitudinal electric field which decelerates the beam electrons at the head of the beam. Eventually these beam electrons lose enough energy that they are lost from the beam, a process called inductive erosion. The physics of these and other beam processes are described in more detail by Lauer *et al.* [1] and by Buchanan [2].

In order to calculate inductive erosion of an electron beam propagating in an ionized channel, all within an ionized background plasma, the problem was idealized by assuming axial symmetry and an ultrarelativistic (rigid rod) beam; that is, the beam electrons are kinematically unaffected by the accompanying EM fields. But the channel and background plasma electrons do respond to these fields. In a reference frame moving with the beam the fields appear to be in steady state, that is, frozen. The frozen field equations [3], coupled with the plasma particle momentum equations, are solved numerically by the appropriately named ARCTIC code [4].

The central assumptions for the computation are

(1) $\gamma \approx \infty$, implying immobile ions, frozen fields.

(2) Steady state in the erosion front frame.

(3) Particles obey individual kinetic equations; fields obey Maxwell equations.

In addition, plasma density was assumed less than 1% of the beam density in testing the code.

The field solution is exponentially decaying outward from the neutralization radius, defined as the radius within which plasma electrons have been expelled to leave a net zero interior charge. In order to impose the conducting wall boundary condition, the calculation integrates the field equations inward from the wall. If this integration has to traverse only a few *e*-folding skin depths, which are inversely proportional to the square root of the plasma density, the procedure can be an explicit one, using the Runga–Kutta–Fehlberg library subroutine. But for large plasma densities and large wall radius, many plasma skin depths exist between the beam and the boundary wall. In this case radial inward integration over a growing solution can lead to numerical instabilities. An explicit algorithm has no control over these instabilities and can lead to unreliable results [4].

To maintain numerical stability when investigating the higher density background plasma regime, the ARCTIC code uses an implicit algorithm. The developed code is described here, along with the steps taken to verify the resulting predictions. The results of numerical and analytic research on inductive erosion and plasma wakefield generation, using ARCTIC and another code, IPROP, are discussed in a separate paper [5].

II. IMPLICIT ALGORITHM

As the electron beam propagates, its head erodes so that the geometric pattern that constitutes the beam front moves somewhat more slowly than the electrons of the beam. We consider the case in which both electrons and front move nearly at the speed of light. In a reference frame moving with the beam front (Galilean transformation) the beam geometric pattern is in steady state, so explicit time derivatives are all zero. The moving frame is Eulerian, with variables referring to specific points in the frame, not to moving particles. In particular, the dimensionless electron axial speed β_z will, in the body of the beam, be small compared with one and will approach zero as the inspection point approaches the beam front.

Derivation of the cylindrically symmetric frozen field and momentum equations appropriate for this problem

0021-9991/96 $18.00

have been presented elsewhere [3]. In dimensionless form, with E_r, E_z, B representing radial and axial electric and azimuthal magnetic fields and J_r, J_z representing radial and axial current densities, they are

$$\frac{\partial E_r}{\partial \zeta} - \frac{\partial B}{\partial \zeta} = -J_r \tag{1}$$

$$\frac{\partial E_z}{\partial r} = J_r \tag{2}$$

$$\frac{1}{r}\frac{\partial}{\partial r} rB = J_z + \frac{\partial E_z}{\partial \zeta} \tag{3}$$

$$(1-\beta_z)\frac{\partial}{\partial \zeta} P_r = -Q \times (E_r - \beta_z B) \tag{4}$$

$$(1-\beta_z)\frac{\partial}{\partial \zeta} P_z = -Q \times (E_z + \beta_r B), \tag{5}$$

where β_r, β_z are the radial, axial particle velocities normalized to the speed of light, $\zeta = v_F t - z$ is the distance back (upstream) from the beam head whose speed in the z direction is $v_F \approx c$, and Q is the particle's charge-to-mass ratio normalized so that $Q = 1$ for electrons. The velocities $\{\beta_i\}$ are related to the normalized momenta $\{P_i \equiv \chi\gamma\beta_i\}$ by $\beta_i = P_i/\sqrt{\chi^2 + P_r^2 + P_z^2}$, where $\chi \equiv 1/4\nu \equiv mc^3/4e\mathscr{I}$ and ν is Budker's parameter. Equations (4) and (5) are the radial and axial momentum equations, respectively. With $\mathscr{I}$ being the (rigid) beam current, and r_b the beam radius, the dimensionless quantities are related to the physical ones (Gaussian units), denoted by tildes, by

$$r, \zeta = \frac{(\tilde{r}, \tilde{\zeta})}{r_b}$$

$$E_r, E_z, B = \frac{cr_b}{4\mathscr{I}} \times (\tilde{E}_r, \tilde{E}_z, \tilde{B})$$

$$J_r, J_z = \frac{\pi r_b^2}{\mathscr{I}} \times (\tilde{J}_r, \tilde{J}_z).$$

In addition to Eqs. (1)–(5), charge conservation is imposed by keeping track in the calculation of the individual charges. The ions are treated either as infinitely massive, immobile charged particles contributing static fields, or as a separate movable particle species with its own charge-to-mass ratio.

The computational grid and the positions at which various quantities are defined is shown in Fig. 1. the radial coordinate r, labeled by index i, goes up vertically, while the longitudinal coordinate ζ (increasing from left to right if the beam is propagating to the left) is labeled by index n. The dashed lines represent the half-step positions. At the beginning of a calculational cycle all the variables are

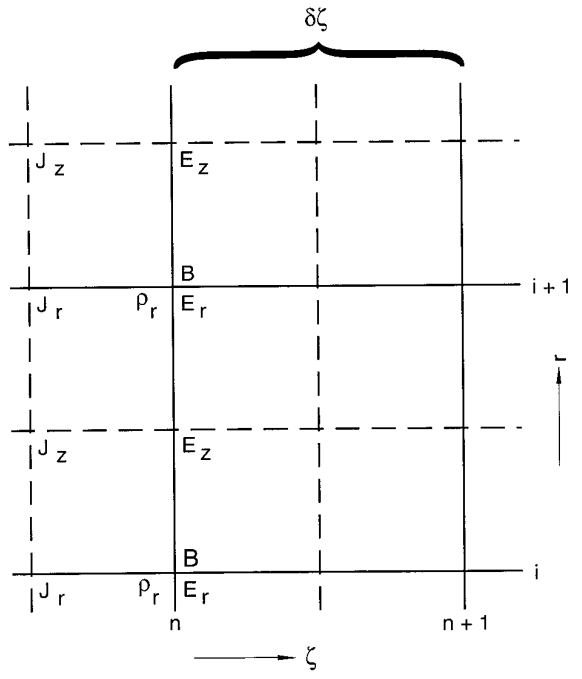

FIG. 1. The ARCTIC computational grid at the beginning of a $d\zeta$ step. The variables shown are known at the locations where they appear. The longitudinal index is n, the radial one is i.

known for every radial position between the beam head (the left edge of the computational grid) and the current value of the longitudinal coordinate ζ, at step n. One computational cycle consists of integrating Eqs. (1)–(5) to advance the known quantities one full step to the right, to step $n + 1$, corresponding to position $\zeta + \delta\zeta$. The "time step" $\delta\zeta$ can vary with ζ.

Note that some quantities are associated with radial and/or longitudinal half-step locations. Since the calculation deals with the discrete charged particles, the accelerations, velocities, and radial positions are associated with the particles rather than with grid locations. With accelerations known at step n, the velocities are known a half step ahead, at $n + \frac{1}{2}$, and the radial positions at $n + 1$. By counting weighted particle densities appropriately, one obtains densities at desired grid locations: J_r at radial full step and longitudinal half-step $(i, n + \frac{1}{2})$, J_z at $(i + \frac{1}{2}, n + \frac{1}{2})$, and charge density ρ_e at (i, n). For any density quantity D that is proportional to the physical particle density, one can write $D \equiv D_\parallel D_\perp$, where $D_\parallel$ represents longitudinal bunching/debunching, and $D_\perp$ represents a radial density. The assumption of a steady state in the near-speed-of-light beam frame dictates that $D_\parallel = 1/(1 - \beta_z)$, so

$$D = \frac{D_\perp}{(1-\beta_z)}. \tag{6}$$

The radial density $D_\perp$ is found directly by counting parti-

cles, multiplied by the appropriate weighting factors, in the different radial intervals.

The calculational algorithm begins with evaluating the current densities at the next half-step, $J_{r_i}^{n+1/2}$ and $J_{z_{i+1/2}}^{n+1/2}$, and the charge density at the next full step, $\rho_{e_i}^{n+1}$. Using the momentum Eqs. (4) and (5) to obtain appropriate coefficient densities (calculated below), the radial current density array is extrapolated to the full step position, $J_r^{(n+1)} = J_r^{n+1/2} + (\partial J_r/\partial\zeta)^{n+1}\delta\zeta/2$. (A superscript or subscript in parentheses means the quantity is extrapolated or interpolated to that location.) The important point here is that the correction-derivative term is taken to depend implicitly on the field quantities, that is, on the as-yet-unknown E_r, B, and E_z at the full step $n+1$. Equation (2) is then integrated radially inward from the conducting boundary wall to give a relation between the still unknown fields at step $n+1$. Equation (3) is then integrated radially out from the axis to give the B field at the half-step $n+\frac{1}{2}$. In principle this result should be extrapolated linearly to the full step position $n+1$, $B^{(n+1)} = 2B^{n+1/2} - B^n$, but this has been found to introduce undamped oscillations. Instead, setting $B^{(n+1)} = B^{n+1/2}$, that is, associating $B^{n+1/2}$ as calculated above with the full step $n+1$, has been found to eliminate these oscillations. Equation (3) thus provides another relation between the still unknown fields E_z^{n+1} and B^{n+1} and the known E_z^n. Finally Eq. (1) constitutes a third relation between known and unknown field values. Since the field values are actually arrays in radial index i, the three relations are matrix equations. These are solved to give the new field quantities at step $n+1$ in terms of the old ones at step n, and in terms of the current components at the half-step $n+\frac{1}{2}$.

With the field quantities known at $n+1$, the momentum equations are applied there, yielding new momenta and particle positions at $n+\frac{3}{2}$ and, hence, also the current density components there. The computational cycle is now complete. The coordinate ζ and index n are incremented, and the cycle begins again.

The above general sketch of the implicit algorithm will now be expanded and described in greater detail.

III. EXTRAPOLATION OF J_r

The total current density J_r of a given particle species is constituted of the moving charged particles flowing in a unit box

$$J_r = \sum_{k\ \text{particles}}^{K} q_k \frac{\beta_{r_k}}{V},$$

where q_k is the normalized charge of particle k, K is the number of particles in the box, and V is the box volume (independent of ζ). Then

$$\frac{\partial J_r}{\partial\zeta} = \frac{1}{V}\langle q\beta_r\rangle\frac{\partial K}{\partial\zeta} + \frac{1}{V}\sum_k^K q_k\frac{\partial\beta_{r_k}}{\partial\zeta}, \tag{7}$$

where the $\langle\ \rangle$ brackets refer to the mean value in the box. Since the particle charges are uncorrelated with their velocities for a given particle species (the charge-to-mass ratio is constant),

$$\langle q\beta_r\rangle = \langle q\rangle\langle\beta_r\rangle,$$

and of course $\langle\beta_r\rangle$ is now the fluid radial velocity of the specie in question. With the definition of the specie charge density $\rho_e \equiv \langle q\rangle K/V$, Eq. (7) becomes

$$\frac{\partial J_r}{\partial\zeta} = \langle\beta_r\rangle\frac{\partial\rho_e}{\partial\zeta} + \frac{1}{V}\sum_k q_k\frac{\partial\beta_{r_k}}{\partial\zeta}. \tag{8}$$

From Eqs. (4) and (5)

$$\begin{aligned}\frac{\partial\beta_r}{\partial\zeta} &= \frac{1}{\gamma}\frac{\partial\gamma\beta_r}{\partial\zeta} - \frac{\beta_r}{\gamma}\frac{\partial\gamma}{\partial\zeta}\\ &= \frac{1}{\chi\gamma}\frac{\partial P_r}{\partial\zeta} - \frac{\beta_r}{\chi\gamma}\frac{\partial}{\partial\zeta}\sqrt{\chi^2 + P_r^2 + P_z^2}\\ &= \frac{Q}{(1-\beta_z)\chi\gamma}[-(1-\beta_r^2)E_r + \beta_z B + \beta_r\beta_z E_z].\end{aligned}$$

Equation (8) now becomes

$$\frac{\partial J_r}{\partial\zeta} = C_1 + C_{E_r}E_r + C_B B + C_{E_z}E_z, \tag{9}$$

where the coefficient densities are

$$C_1 \equiv \langle\beta_r\rangle\frac{\partial\rho_e}{\partial\zeta} \tag{10}$$

$$C_{E_r} \equiv -\frac{Q}{V}\sum_k\frac{(1-\beta_{r_k}^2)q_k}{(1-\beta_{z_k})\gamma_k} \tag{11}$$

$$C_B \equiv \frac{Q}{\chi V}\sum_k\frac{q_k\beta_{z_k}}{(1-\beta_{z_k})\gamma_k} \tag{12}$$

$$C_{E_z} \equiv \frac{Q}{\chi V}\sum_k\frac{q_k\beta_{r_k}\beta_{z_k}}{(1-\beta_{z_k})\gamma_k}. \tag{13}$$

If there is more than one specie, (Eq. 9) is easily generalized by redefining the coefficients (Eqs. (10)–(13)) to be the sums over species of the coefficients as defined above for each specie:

$$C_1 = \sum_{\sigma\,\text{species}} \langle\beta_r\rangle_\sigma \frac{\partial}{\partial\zeta}\rho_{e_\sigma},$$

$$C_{E_r} = -\frac{1}{\chi V}\sum_{\sigma\,\text{species}} Q_\sigma \sum_k^{K_i} \frac{(1-\beta_{r_k}^2)q_k}{(1-\beta_{z_k})\gamma_k}, \quad \text{etc.}$$

The above sums are over moving species, that is, channel and background plasma electrons, and, if so treated, the plasma ions, but the beam electrons are not included. For any given specie, the terms to be summed in expressions (11)–(13) are simply evaluated at the radial boundaries i and half-step $n+\frac{1}{2}$ by computing appropriately weighted densities there. For Eq. (10) it is necessary to evaluate a fluid radial velocity at the half-step $\langle\beta_{r_i}\rangle^{n+1/2}$, and charge densities at the full step positions $\rho_{e_i}^n, \rho_{e_i}^{n+1}$ to obtain the derivative and final expression at the half step $n+\frac{1}{2}$. The longitudinal electric field at the radial boundary is obtained by averaging the neighboring values, $E_{z_i}^{n+1} = \frac{1}{2}(E_{z_{i-1/2}}^{n+1} + E_{z_{i+1/2}}^{n+1})$. Finally, the extrapolated radial current density at the full step $n+1$ is

$$J_{r_i}^{(n+1)} = J_{r_i}^{n+1/2} + \tfrac{1}{2}\delta\zeta[C_{1_i}^{n+1/2} + C_{E_{r_i}}^{n+1/2}E_{r_i}^{n+1} + C_{B_i}^{n+1/2}B_i^{n+1} + \tfrac{1}{2}C_{E_{z_i}}^{n+1/2}(E_{z_{i-1/2}}^{n+1} + E_{z_{i+1/2}}^{n+1})]. \tag{14}$$

Henceforth we simplify notation by writing quantities in vector and matrix form, the elements corresponding to different radial indices i. Thus all the physical quantities $E_r, B, E_z, J_r, J_z, \beta_r, \beta_z$, etc. become vectors, with the first elements corresponding to locations closest to, but off the axis, while coefficients and operators become matrices. The coefficients C_{E_r} and C_B are diagonal square matrices

$$\mathbf{C}_B = \begin{pmatrix} C_{B_1} & & & 0 \\ & C_{B_2} & & \\ & & \ddots & \\ 0 & & & C_{B_M} \end{pmatrix}, \quad \text{etc.},$$

where M is the number of radial cells, and the coefficient $\mathbf{C}_{E_z}$ is a two-diagonal matrix (with diagonal = superdiagonal)

$$\mathbf{C}_{E_z} = \begin{pmatrix} C_{E_{z_1}} & C_{E_{z_1}} & & & 0 \\ & C_{E_{z_2}} & \ddots & C_{E_{z_2}} & \ddots \\ 0 & & & & C_{E_{z_M}} \end{pmatrix}$$

where element

$$C_{E_{z_i}} \equiv \left(\frac{1}{2}\sum_k \frac{\beta_{r_k}\beta_{z_k}}{(1-\beta_{z_k})\chi\gamma_k}\rho_{e_k}\right)$$

at radial position i. The constant C_1 is an M-element array.

IV. DIFFERENCE EQUATIONS

In difference form Eq. (2) is

$$E_{z_{i+1/2}}^{n+1} = E_{z_{i+3/2}}^{n+1} - J_{r_{i+1}}^{(n+1)}\,\delta r_{i+1},$$

where δr_i is the radial distance between the cell centers sharing radial boundary i. The interval nearest the wall, δr_{M+1}, is just half the width of the outermost cell, from cell center to wall. In matrix form this equation can be written

$$\mathbf{A}E_z^{n+1} = -\mathbf{D}J_r^{(n+1)}, \tag{15}$$

where matrices $\mathbf{A}$ and $\mathbf{D}$ are

$$\mathbf{A} \equiv \begin{pmatrix} 1 & -1 & & & 0 \\ & 1 & -1 & & \\ & & 1 & -1 & \\ 0 & & & \ddots & \end{pmatrix}$$

$$\mathbf{D} \equiv \begin{pmatrix} \delta r_2 & & & & 0 \\ & \delta r_3 & & & \\ & & \delta r_4 & \ddots & \\ 0 & & & & \delta r_{M+1} \end{pmatrix}.$$

Using Eq. (14) in matrix form, Eq. (15) becomes

$$\mathbf{A}E_z^{n+1} = -\mathbf{D}J_r^{n+1/2} - \tfrac{1}{2}\delta\zeta\,\mathbf{D}(C_1^{n+1/2} + \mathbf{C}_{E_r}^{n+1/2}E_r^{n+1} + \mathbf{C}_B^{n+1/2}B^{n+1} + \mathbf{C}_{E_z}^{n+1/2}E_z^{n+1}). \tag{16}$$

Equation (1) in difference form is

$$E_r^{n+1} = B^{n+1} + E_r^n - B^n - \delta\zeta J_r^{n+1/2}. \tag{17}$$

Eliminating E_r^{n+1} between Eqs. (16) and (17) gives

$$\begin{aligned}(\mathbf{A} + \tfrac{1}{2}\delta\zeta\,\mathbf{D}\mathbf{C}_{E_z}^{n+1/2})E_z^{n+1} &= -\mathbf{D}J_r^{n+1/2} - \tfrac{1}{2}\delta\zeta\,\mathbf{D}C_1^{n+1/2} \\ &\quad - \tfrac{1}{2}\delta\zeta\,\mathbf{D}(\mathbf{C}_{E_r}^{n+1/2} + \mathbf{C}_B^{n+1/2})B^{n+1} \\ &\quad - \tfrac{1}{2}\delta\zeta\,\mathbf{D}\mathbf{C}_{E_r}^{n+1/2}(E_r^n - B^n - \delta\zeta J_r^{n+1/2}).\end{aligned} \tag{18}$$

In difference form Eq. (3) (after setting $B^{(n+1/2)} = B^{n+1}$ as explained earlier) is

$$r_{i+1}B_{i+1}^{n+1} = r_i B_i^{n+1} + r_{i+1/2}\,\delta r_{i+1/2}\left[J_{z_{i+1/2}}^{n+1/2} + \left(\frac{\partial E_z}{\partial \zeta}\right)_{i+1/2}^{n+1/2}\right]. \tag{19}$$

In principle the last term should just be (omitting subscripts)

$$\left(\frac{\partial E_z}{\partial \zeta}\right)^{n+1/2} = \frac{1}{\delta\zeta}(E_z^{n+1} - E_z^n).$$

When the time step $\delta\zeta$ becomes small this expression can lead to numerical instability. A more smoothly varying expression that eliminates the instability is used instead:

$$\left(\frac{\partial E_z}{\partial \zeta}\right)^{n+1/2} = \frac{\alpha}{\delta\zeta}(E_z^{n+1} - E_z^n) + (1-\alpha)\left(\frac{\partial E_z}{\partial \zeta}\right)^{n-1/2}. \tag{20}$$

This expression for the derivative is an interpolation between its previous value (corresponding to $\alpha = 0$) and the instantaneous one ($\alpha = 1$). The nominal value of parameter α is 1. But when time step $\delta\zeta$ is smaller than some interval ζ_R, α is set equal to the ratio $\delta\zeta/\zeta_R$. ζ_R is a resolution time scale and is set equal to some small fraction, normally $\frac{1}{8}$, of a plasma period in the channel. Since $\delta\zeta$ can vary during the calculation, so can α. It was found empirically that the chosen value of ζ_R eliminated the aforementioned numerical instability and also gave stable results largely insensitive to the exact value of ζ_R. However, no detailed studies of variability with ζ_R were performed.

Define $\mu_i \equiv r_{i+1/2}\,\delta r_{i+1/2}$, and the diagonal matrices

$$\mathbf{U} \equiv \begin{pmatrix} \mu_1 & & 0 & \\ & \mu_2 & & \\ 0 & & \mu_3 & \ddots \end{pmatrix}$$

$$\mathbf{R} \equiv \begin{pmatrix} r_2 & & 0 & \\ & r_3 & & \\ 0 & & r_4 & \ddots \end{pmatrix};$$

then Eq. (19) in matrix notation becomes

$$\mathbf{B}B^{n+1} = J_z^{n+1/2} + \frac{\alpha}{\delta\zeta}(E_z^{n+1} - E_z^n) + (1-\alpha)\left(\frac{\partial E_z}{\partial \zeta}\right)^{n-1/2}, \tag{21}$$

where the matrix $\mathbf{B} \equiv \mathbf{U}^{-1}\mathbf{A}^{\mathrm{T}}\mathbf{R}$, and $\mathbf{A}^{\mathrm{T}}$ is the transpose of $\mathbf{A}$.

Eliminating E_z^{n+1} between Eqs. (18) and (21) gives an expression for B^{n+1} in terms of previously determined quantities:

$$\begin{aligned}\mathbf{M}B^{n+1} = {} & -\alpha W + \left(\mathbf{A} + \frac{1}{2}\,\delta\zeta\,\mathbf{D}\mathbf{C}_{E_z}\right) \\ & \times \left[J_z^{n+1/2} + (1-\alpha)\left(\frac{\partial E_z}{\partial \zeta}\right)^{n-1/2}\right] \\ & -\frac{\alpha}{2}\mathbf{D}[C_1 + \mathbf{C}_{E_z}E_z^n + \mathbf{C}_{E_r}(E_r^n - B^n - \delta\zeta J_r^{n+1/2})].\end{aligned} \tag{22}$$

Here C_1 and all the $\mathbf{C}$ coefficients are understood to have superscript $n + \frac{1}{2}$. The matrix $\mathbf{M}$ is defined by

$$\mathbf{M} \equiv \mathbf{A}\mathbf{B} + \tfrac{1}{2}\mathbf{D}[\delta\zeta\,\mathbf{C}_{E_z}\mathbf{B} + \alpha(\mathbf{C}_{E_r} + \mathbf{C}_B)] \tag{23}$$

and the vector W is

$$W \equiv \frac{(\mathbf{A}E_z^n + \mathbf{D}J_r^{n+1/2})}{\delta\zeta}. \tag{24}$$

By analogy with Eq. (16) the following relation should apply as $\delta\zeta \to 0$:

$$\mathbf{A}E_z^n = -\mathbf{D}J_r^{n+1/2} + \tfrac{1}{2}\,\delta\zeta\,\mathbf{D}(C_1 + \mathbf{C}_{E_r}E_r^n + \mathbf{C}_B B^n + \mathbf{C}_{E_z}E^n).$$

So as $\delta\zeta \to 0$, W should approach the limiting value (superscripts for C_1 and the $\mathbf{C}$'s are still $n + \frac{1}{2}$)

$$W_L \equiv \tfrac{1}{2}\mathbf{D}(C_1 + \mathbf{C}_{E_r}E_r^n + \mathbf{C}_B B^n + \mathbf{C}_{E_z}E_z^n). \tag{25}$$

In the calculation the value of W is made equal to its defined value (Eq. (24)) for steps $\delta\zeta$ larger than some small critical value ζ_* and changes smoothly to the limiting value W_L as $\zeta_* > \delta\zeta \to 0$. In derivative form,

$$W_L = \frac{1}{2}\frac{\partial J_r}{\partial \zeta}\,\delta r.$$

The matrix $\mathbf{M}$ in Eq. (22) is tridiagonal and of order N, the number of radial cells in the calculation. In the calculation Eq. (22) is inverted numerically, giving the new array B^{n+1}. Then Eq. (17) gives the array E_r^{n+1} and Eq. (21) gives the array E_z^{n+1}, from which $(\partial E_z/\partial\zeta)^{n+1/2}$ is calculated using Eq. (20).

With the fields now known at step $n + 1$, the momentum Eqs. (4) and (5) are applied to advance the particle veloci-

ties to the half step $n + \frac{3}{2}$. From that the particle positions are advanced to half-step $n + \frac{3}{2}$:

$$R_i^{(n+3/2)} = R_i^{n+1} + \beta_{r_i}^{n+3/2} \frac{\delta\zeta/2}{1 - \beta_{z_i}^{n+3/2}}$$

and, similarly, to step $n + 2$. The radial density of these particles is used in Eq. (6) to compute the corresponding charge densities. Then the whole computational cycle is repeated.

V. GRID SELECTION

The background plasma densities typically are small, compared with the beam electron density. On the other hand, the radial region of interest is large compared with the beam radius. To deal with this large radius range the radial cells were picked to increase in thickness with the radius. With a nearly constant thickness δr near the axis, at large radius r the increment δr varied proportionally to r. Far from the beam the amount of plasma in a radial cell thus increased as r^2. For large plasma densities and large wall radii, this meant that cells at large radius could numerically contain more charge than the beam itself. But as noted in the Introduction, this region beyond the neutralization radius is an electrical shielding layer, analogous to a Debye sheath, that is now many skin depths thick. To assure that the fields, growing exponentially on inward integration, stay properly resolved, the cell thickness in this region is chosen to keep the maximum possible charge in a cell less than a specified fraction f of the beam charge. So at smaller radii the cell size is allowed to increase with the radius as originally prescribed until fraction f is exceeded, and beyond that the size decreases to keep the cell area constant: $r\ \delta r = \text{const}$. Typically $0.2 \leq f \leq 0.5$ has been found to work well. In a given problem, depending on beam current, background plasma density, and wall radius, there may be just one region of cell thickness variation, in which all cells have less than fraction f of the beam charge, or two regions of cell thickness variation, in which the cells in the outer region all have a constant fraction f of the beam charge.

VI. INDUCTIVE EROSION RATE IN THE FROZEN FIELD APPROXIMATION

The model of inductive beam erosion assumes that in the frame moving with the erosion front the fields and plasma flow trajectories are in steady state. In that frame, the beam electrons far upstream from the head are moving forward (toward the front) at the erosion speed $v_E \equiv c\beta_E = c(\beta_\infty - \beta_F)$, where β_∞ and β_F are the dimensionless velocities of the beam far upstream (hence, the ∞ symbol) and the moving frame, respectively, measured in the lab frame. As the beam energy γ is increased the normalized erosion speed is decreased so that the erosion front is moving at almost the same speed as the beam. The frozen field approximation applies in the erosion front frame. In particular a longitudinal electric field E_z is established that is steady state in the erosion frame. Define the potential φ, with $\varphi = 0$ at the erosion front, through the relation

$$\frac{e}{mc^2} E_z \equiv -\frac{\partial\varphi}{\partial z} = \frac{\partial\varphi}{\partial z'}, \tag{26}$$

where $z' \equiv \beta_F ct - z$ is the longitudinal coordinate in the frame moving with the erosion front. The potential φ, averaged over the beam cross section, is calculated by ARCTIC as a function of axial position along the axis. This quantity is plotted by ARCTIC under the label "normalized erosion rate," because it is equal to $(\gamma_\infty - \gamma_F)\beta_E$.

If a continuous beam has been propagating a long distance so that the erosion front has moved several plasma oscillation wavelengths up the beam, in the frame of the erosion front the beam will have been moving forward through a fixed longitudinal wake field pattern E_z, and so it has been accelerated and decelerated in accordance with the potential distribution $(mc^2/e)\varphi(z')$. The dimensionless potential $\varphi(z')$, therefore, is simply a measure of the decrease of the beam γ at z' through $\beta_E d(\gamma\beta)/dz' = d\varphi/dz$. Since far upstream φ approaches a constant φ_∞, the value of $\varphi_\infty/(\gamma_\infty - \gamma_F)$, where γ_∞ is the initial beam energy, gives the erosion rate β_E. γ_F accounts for the reduced beam energy at the erosion front where the beam velocity is $\beta(z' = 0) = \beta_F$. This is discussed in more detail in a separate paper [5].

VII. CALCULATIONS AND COMPARISONS

The parameter range over which the code has been tested is beam current $\mathcal{I}$ between 1 and 10 kA, beam radius 1 to 10 cm, ratio λ_c of density to beam density of 0.1 to 1.0, ratio f_p of background plasma density to beam density of 10^{-10} to 10^{-2}, and wall radius 10 to 1000 beam radii. In performing the calculations with the ARCTIC code, several computational parameters need to be specified, including radial cell sizes, longitudinal step sizes, the exponent m of the supergaussian initial channel density distribution e^{-r^m}, and the averaging fraction α used in calculating the derivative $\partial E_z/\partial\zeta$. In a few cases with physical parameters representative of the range of interest, extensive calculations were made for each case using different computational parameters. It was found that results changed negligibly (less than a few percentages) when

a. radial cell size on axis was varied between 0.025 and 0.1 of the beam radius;

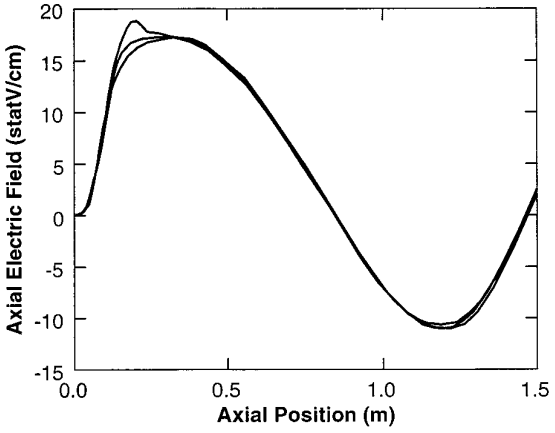

FIG. 2. Axial distributions of E_z, calculated by ARCTIC, for different values of the limiting parameter F (see text): $F = 0.2, 0.5, 1$. The initial peak is larger for larger F values.

b. the initial longitudinal step size $\delta\zeta$ was varied between 0.01 and 0.5 of the channel plasma period;

c. channel density profile was made sharper: from nominal distribution $e^{-r^{10}}$ to $e^{-r^{20}}$.

The time step during a calculation is limited by several factors. It is kept small enough to resolve the current rise time, electric field changes, and plasma oscillations. In addition, there is a requirement that no particle may move radially, during one time step, more than some specified fraction F of a radial cell. The effect of the value of F on the calculation results was examined by repeating the calculation for different values of F, including $F = 0.1, 0.2, 0.5, 1$, and 2. For values of F larger than about 1, restraints on the time step DT are imposed by resolution requirements, and the value of F becomes moot. For smaller values of F the particle trajectories are almost unaffected. The main differences appear in the electric field distributions near the head of the beam. Larger values of F cause the longitudinal electric field at the front of the beam to increase faster than it should and attain higher values. Figure 2 shows the axial distribution of E_z at different radii for F values of 0.2, 0.5, and 1. The solid line, usually the envelope, refers to a radius near the beam radius. The distribution becomes noticeably distorted for $F \gtrsim 0.5$, although the trajectories and erosion speed are little affected.

ARCTIC results were compared with both theory and PIC simulations. The ''normalized erosion rate'' computed by ARCTIC (defined in Section VI) showed good agreement (within 10%) with the same quantity predicted by theory [5] over order-of-magnitude ranges of beam currents I and beam-to-chanel density ratios f_P, and four orders of magnitude range of background plasma density. As described by Mostrom *et al.* [5], the theory—valid also for nonrelativistic beams—was compared and agreed well with both experimental results and PIC simulations. Because of their expense, the stimulations using IPROP [6]—a three-dimensional, particle-in-cell (PIC) code—were generally made to conform with experimental parameters, i.e., with low values of γ not consistent with ARCTIC. But one high-γ IPROP simulation was performed with a 2 kA, 1-cm radius beam propagating in a 2-cm radius channel. Line density ratio of the channel was $\lambda_c = 0.5$, background plasma density was 0.009 of the beam electron density, beam rise time was $ct_R = 50$ cm, wall radius was 64 cm, and cylindrical symmetry was assured by using only the $m = 0$ mode. IPROP presents particle positions at successive time steps, with channel and plasma electrons initially distributed uniformly in the longitudinal and radial directions (but with a density change between channel and plasma at the channel radius). The lab-frame snapshot in Fig. 3b shows these electrons after the beam, injected from the right side, has almost reached the left side of the simulation box, by which time most of the startup transients have decayed. Figure 3a shows the electron streamlines computed in ARCTIC's beam frame (but recall that the transformation used was Galilean, so no longitudinal distortion was introduced). Figure 4 shows the corresponding E_z distributions on the axis. The qualitative agreement is good. The difference is caused mainly by boundary conditions: in IPROP the field measuring position is 1.5 m from the metal surface through which the beam was injected. These comparisons gave confidence that ARCTIC results can provide needed guidance for understanding beam erosion, both experimentally and analytically [5].

ARCTIC has also been used to investigate plasma wakefields induced by an electron beam propagating through a background plasma. Because ARCTIC runs so fast (orders of magnitude faster than IPROP, which must follow more detailed time-dependent and finite-γ effects) and with spatial resolutions much finer than practical with a PIC code, we were able to carry out hundreds of runs on a Mac IIci personal computer over a wide parameter regime and statistically fit the results of the wave amplitude to a phenomenological model. This in turn was used to predict a parameter regime where the wakefields were least disruptive to the beam. This was verified by IPROP and explained by an analytic model [7].

VIII. CONCLUSION

The development and application of the ARCTIC code has proved to be very successful. The implicit algorithm was crucial in allowing the simulation of beam propagation through large volumes of background plasma. This allowed accurate modeling of beam inductive erosion and plasma wakefields. The code ran sufficiently fast that tens of runs per day could be accomplished on a modest desktop per-

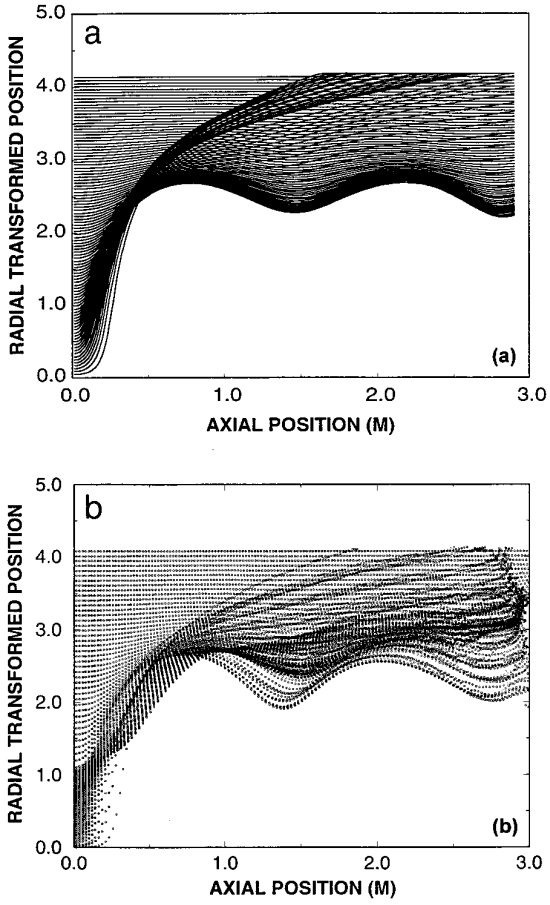

FIG. 3. Comparisons of (a) plasma streamlines by ARCTIC and (b) plasma electron positions by IPROP, resulting from a 2 kA, 1-cm radius beam propagating in a 2-cm radius channel with $\lambda_c = 0.5$ and background plasma density of 1.2×10^9 cm^{-3}. The beam, which is moving to the left, has a rise time of 50 cm. The comparison is qualitative since exact correspondence in resolution and boundary conditions is not practical. In (b) the curled particle tracks at the right are produced by the conducting boundary condition at that boundary. One feature noticable in all the PIC simulations that is not seen in ARCTIC simulations is the presence of particles at lower radii when the plasma is first blown out. This small discrepancy is not fully understood but may be caused by transients not seen in the steady-state ARCTIC simulations.

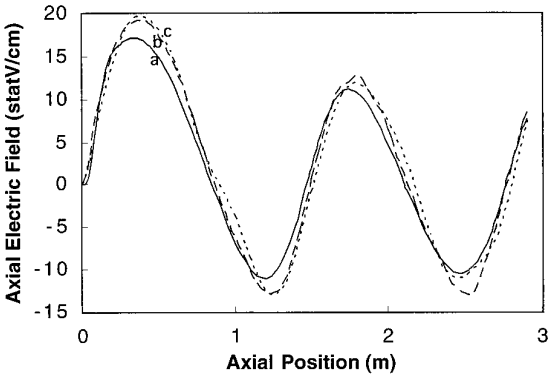

FIG. 4. Comparisons of axial distributions of E_z as calculated by (a) ARCTIC and (b), (c) IPROP for the same parameters as in Fig. 3. (b) and (c) show the smoothed values of E_z and differ in that cell sizes in (c) were halved both axially and radially from those in (b). In the IPROP simulation, the field measuring position was 1.5 m downstream from a conducting boundary through which the beam was injected.

sonal computer, and it allowed an efficient interaction among theory, numerical simulation, empirical modeling, and experiments.

APPENDIX: RADIAL ZONING

To minimize the number of radial cells, a radially nonuniform distribution of cell sizes is used, with cells becoming larger at larger radii. Coupled with the radial weight factor r, the cell volumes increase radially as does the amount of mass contained. For sufficiently large wall radii it is possible for a cell to contain more charge than the entire beam charge. To avoid this situation, which could introduce inaccuracies, the radial cell size is constrained so that the charge it contains does not exceed a fraction C_{rat} of the beam charge. In the inner region where this constraint does not apply the transformed radial coordinate x is related to the radius r by

$$x = r_b * \ln\left(1 + \frac{r}{r_b}\right). \tag{A1}$$

The transformed cell size δx is related to actual cell size δr by

$$\delta x = \frac{\delta r}{1 + r/r_b}. \tag{A2}$$

The radius r^*, at which a cell would initially contain as plasma electrons a fraction C_{rat} of the beam charge, is

$$r^* = \tfrac{1}{2}(\sqrt{1 + 2C_{\text{rat}}/f_p\,\delta x} - 1), \tag{A3}$$

where f_p is the ratio of plasma electron density to beam electron density. For radii less than r^* the relation between r and x is just that of Eq. (A1), so Eq. (A2) applies. For larger radii the cell size δr is adjusted so the cells contain just C_{rat} times the beam charge:

$$\delta r = \frac{r_b}{2r}\frac{r_b}{C_{\text{rat}} f_p}. \tag{A4}$$

Requiring a constant interval δx in the transformed coordinate gives the relation

$$\frac{dx}{dr} = 2\frac{r}{r_b}\frac{\delta x}{r_b} C_{\text{rat}} f_p. \tag{A5}$$

Integrating from r^* to r gives

$$x = x^* + \delta x\, C_{\text{rat}} f_p \left[\left(\frac{r}{r_b}\right)^2 - \left(\frac{r^*}{r_b}\right)^2 \right], \tag{A6}$$

where x^* corresponds to r^*, according to Eq. (A1).

The number of radial cells required is

$$N = \frac{x_w}{\delta x},$$

where x_w refers to the wall radius r_w, and is given by Eq. (A1) if $r_w \le r^*$ and by Eq. (A6) if $r_w > r^*$:

$$N = \begin{cases} \dfrac{r_b}{\delta x} \ln\left(1 + \dfrac{r_w}{r_b}\right) & \text{if } r_w < r^* \\ \dfrac{f_p}{C_{\text{rat}}} \left[\left(\dfrac{r_w}{r_b}\right)^2 - \left(\dfrac{r^*}{r_b}\right)^2 \right] + \dfrac{r_b}{\delta x} \ln\left(1 + \dfrac{r^*}{r_b}\right) & \text{if } r^* < r_w. \end{cases}$$

Trials have shown that a value $\delta x / r_b \approx 0.05$ gives good radial resolution and still keeps the number N of radial cells to a manageable number $50 \lesssim N \lesssim 200$.

REFERENCES

1. E. J. Lauer, R. J. Briggs, T. J. Fessenden, R. E. Hester, and E. P. Lee, *Phys. Fluids* **21,** 1344 (1978).
2. H. L. Buchanan, *Phys. Fluids* **30,** 221 (1987).
3. M. Lampe, T. Sharp, R. Hubbard, E. P. Lee, and R. Briggs, *Phys. Fluids* **27,** 2921 (1984); E. P. Lee, LLNL Report VCID-17286, 1976 (unpublished).
4. M. A. Mostrom and B. S. Newberger, *Bull. Am. Phys. Soc.* **31,** 1399 (1986); B. Newberger, M. Mostrom, and B. Godfrey, AMRC-N-354, November 1986 (unpublished); M. Mostrom, B. Godfrey, B. Newberger, and S. Arman, AMRC-N-360, February 1987 (unpublished), Mission Research Corporation, Albuquerque, NM.
5. M. A. Mostrom, D. Mitrovich, D. R. Welch, and M. M. Campbell, *Phys. Plasmas,* in press.
6. B. B. Godfrey and D. R. Welch, in *Twelfth Conference on Numerical Simulation of Plasmas, San Francisco, CA, 1987,* paper CM1; AMRC-R-690, 1985 (unpublished).
7. D. R. Welch and M. A. Mostrom, in preparation.